

AN EXPERIMENTAL ANALYSIS OF THE FLOW STRUCTURE IN VARIOUS CONFIGURATIONS OF A CIRCULAR-PLANAR SOFC FUEL CHANNEL

REMIGIUSZ NOWAK

JANUSZ S. SZMYD

*AGH-University of Science and Technology, Faculty of Energy and Fuels, Kraków, Poland
e-mail: remigius@agh.edu.pl; janusz@agh.edu.pl*

In the presented paper, the authors focus on the analysis of flow structure in various configurations of a circular-planar SOFC fuel channel. The research was carried out on the premise that a proper channel design would help minimize the thermal stress in the cell, which is affected by the heat generated and consumed by the reforming, water gas-shift and hydrogen consumption reactions. For the measurement process, PIV method was used to calculate the velocity fields, and an extensive error analysis was done to evaluate the accuracy of the calculated velocities.

Key words: particle image velocimetry, error analysis, flow distribution, SOFC

Nomenclature

\hat{I}^*, \hat{I} – Fourier transform and complex-conjugate of Fourier transform of I , respectively

CC, NCC – cross-correlation function and normalized cross-correlation function

d – length of each P_n plane, [m]

d_H – hydraulic diameter, [m]

I – intensity distribution

l, l_0 – in axis total and fractional channel length, [m]

Re – Reynolds number

V, \bar{V} – velocity and average velocity, [m/s]

x – fractional length of each P_n plane, [m]

ΔH^0 – standard enthalpy change, [kJ/mol]

ΔV – velocity difference, [m/s]

Greek symbols

η – dynamic viscosity, [kg/(m s)]

ν – kinematic viscosity, [m²/s]

ρ – density, [kg/m³]

σ – RMS error (standard deviation), [m/s]

1. Introduction

The world suffered the global oil crisis in 1973, and now, with constantly increasing oil prices and a decreasing number of natural energy sources, there is a need for alternative means of producing electric energy. One of the most promising and extensively developed methods is the fuel cell technology. A fuel cell is basically an electrochemical device that directly converts the chemical energy of a fuel into an electric current. As it reaches efficiencies of about 50% and as the secondary product generates steam, it is believed to be a clean and efficient energy source for our present and future society. From the wide range of different fuel cell types, one of the most interesting and broadly studied is the Solid Oxide Fuel Cell (SOFC), which is designed to operate in medium and high temperatures of about 800-1000°C (IT-SOFC, HT-SOFC). In an SOFC, the hydrogen is used as a fuel for the fuel cell but its high operating temperature allows it to operate on hydrocarbon fuels such as methane.

An important aspect in the construction process of each SOFC cell is the proper design of the fuel and air distribution channel. As Singhal and Kendall (2006) and Atkinson and Sun (2007) have said, the cell designs including material properties and operating conditions have a substantial influence on the thermal stresses that may occur in the cell during operation. It is particularly important for the cells with direct internal reforming (DIR) where the cooperating endothermic reforming reaction ($\Delta H_{1073\text{K}}^0 = 242$ kJ/mol), exothermic water gas shift ($\Delta H_{1073\text{K}}^0 = -38.6$ kJ/mol) and hydrogen conversion ($\Delta H_{1073\text{K}}^0 = -250$ kJ/mol) reactions are among those responsible for the rise in the temperature difference along the reaction channels (Laurencin *et al.*, 2006). This phenomenon was also studied by Ho *et al.* (2008) who observed that the fuel cooled by the reforming reaction at the inlet to the cell is gradually warmed up as a consequence of the two above reactions. Moreover,

Laurencin *et al.* (2006) concluded that "the Nusselt number depends strongly on the geometry of the gas channels" so the channel design is also responsible for the relationship between the conductive and convective heat transfers in the cell. It is on these grounds that we decided to study the three different configurations of the circular-planar SOFC to uncover the possibilities for maintaining the temperature difference and, therefore, also the thermal stresses at acceptable levels. In the paper, it was assumed that the rates of chemical reactions in the cell depend on the fuel velocity distribution in the fuel and air distribution channels.

Particle Image Velocimetry (PIV) was used for the velocity field calculations; its bases are described in the next section. As PIV is based on the statistical calculations of velocity vectors, an accurate error analysis is presented in the closing section of the paper.

2. Measurement technique

Particle Image Velocimetry was broadly described by Keane and Adrian (1992), Westerweel (1997) and Raffel and Willert (2007). Figure 1 presents an overview of this measurement process.

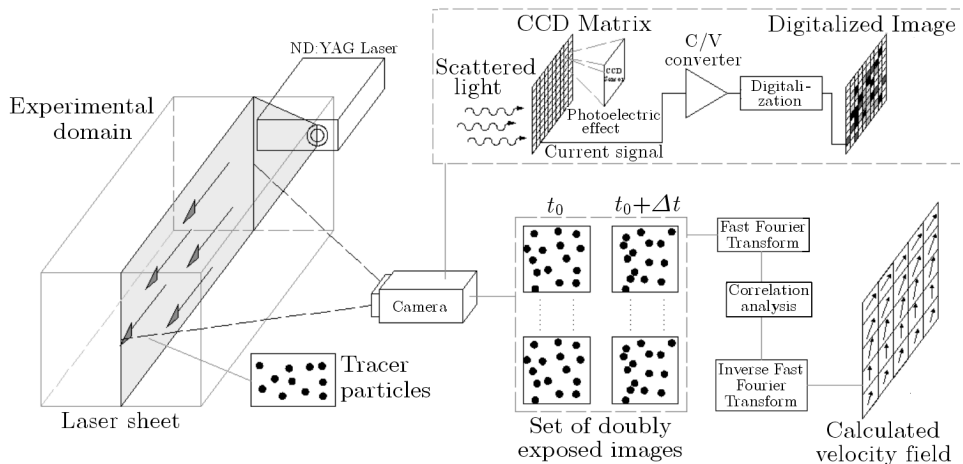


Fig. 1. General representation of the Particle Image Velocimetry (PIV) measurement technique

To determine the flow in PIV measurement, a set of tracer particles that fulfill exact requirements have to be added to the fluid being studied. There is a broad range of different types of tracer particles suitable for specific expe-

rimental setups (Melling, 1997). The main features that decide about their application to specific process are the scattering factor (visibility) and their density (flow tracking). With PIV, the image is recorded on the CCD camera matrix mostly in the form of double frame images that, in the case of a camera resolution of 2048×2048 pixels, consist of about 4 million CCD sensors (each diital pixel = 1 sensor). The continuous voltage signal captured by each sensor is then converted by the C/I converter to a digital image. During the conversion process the continuous voltage signal is transformed into discrete digital domain $M \times N \times k^1$ where the M and N values represent the number of pixels in the horizontal and vertical dimension while k is the bit rate of the digital image, which represents the number of gray scale values that can be assigned to each pixel (Fig. 2a). In the next step each of the doubly exposed images is divided into interrogation windows of size that may vary from 4×4 to 128×128 pix (Fig. 2b). Every window is then described by the $I(i, j)$ function

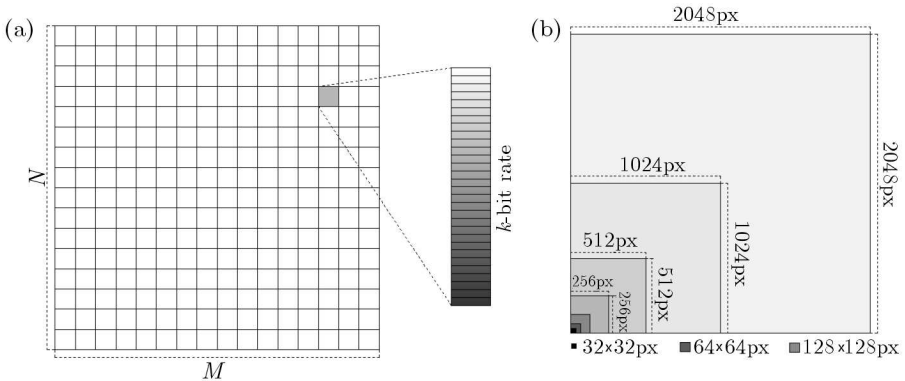


Fig. 2. (a) Representation of the CCD chip digital domain, (b) interrogation window sizes in comparison with 256×256 - 2048×2048 image sizes

that presents the intensity distribution over the window area. Particularly, the function $I_1(i, j)$ represents the intensity distribution in image 1 and the function $I_2(i, j)$ in image 2. Then, in the calculation stage all of the interrogation windows from the second image are compared with the ones from the first one. The comparison process is realized by the cross-correlation function, which in the spatial domain may be represented by the following equations

$$\begin{aligned}
 CC(i, j) &= I_1(i, j) \otimes I_2(i, j) \\
 CC(i, j) &= \sum_i \sum_j I_1(i, j) I_2(i - m, j - n)
 \end{aligned}
 \tag{2.1}$$

¹i.e 8 bit image is the image where each pixel can have a gray scale value in the 0-256 range.

In Eq. (2.1) the m and n variables represent the interrogation window shift value in the i and j direction, respectively. The aim of the calculations is to determine the $CC(i, j)$ correlation function for each pair of interrogation windows. The highest value of $CC(i, j)$ represents the most probable fluid displacement vector (Fig. 3). Mostly before the calculation phase, the functions $I_1(i, j)$ and $I_2(i, j)$ are transformed by the Fast Fourier Transform (FFT) into the frequency domain where the sum is replaced by simple multiplication operations

$$I_1(i, j) \otimes I_2(i, j) \Leftrightarrow \text{FFT}^{-1} \left(\widehat{I}_1(u, v) \cdot \widehat{I}_2^*(u, v) \right) \quad (2.2)$$

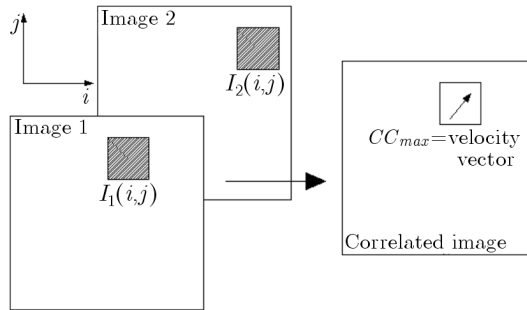


Fig. 3. Schematic representation of the idea of PIV calculation process

This is done mainly due to the time required for calculations. Calculations for the window sizes of the $M \times M$ and $N \times N$ pixels in the spatial domain require about $N^2(M - N + 1)^2$ operations. The same process in the frequency domain requires only $12M^2 \log 2M$ operations (Lewis, 1995). As the $CC(u, v)$ displacement function in the frequency domain is determined, the reverse FFT is applied to transform the results back into the spatial domain, which results in the final $CC(i, j)$ value representing the most probable displacement of the tracer particles.

3. Experimental procedure

3.1. Problem description

In all planar fuel cells the interconnect part is the element responsible for proper flow distribution of the fuel and oxidant fluids on both the anode and cathode sides of the cell. At present, several interconnect configurations can

be found in the literature: z-flow, serpentine-flow, co-/counter-/cross-flow configurations for planar and radial-flow, and spiral-flow for circular-planar cells (Singhal and Kendall, 2006). In this paper, three kinds of radial-flow interconnect configurations have been tested; they are similar to the solutions proposed by the Hexis Ltd.² company. The exact geometric shape and size of the examined channels are presented in Fig. 4. The outer diameters of all the presented

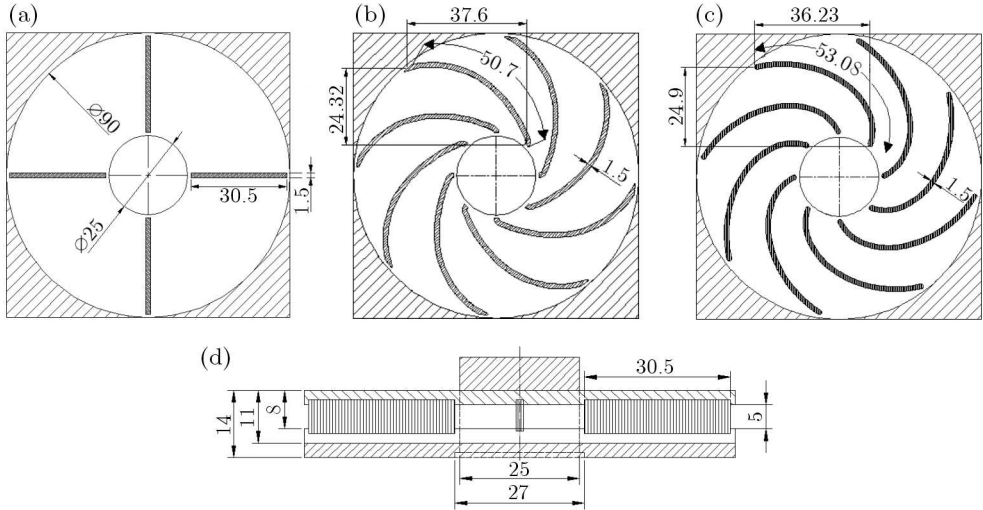


Fig. 4. Investigated geometries; (a) channel 1, (b) channel 2, (c) channel 3, (d) channel 1 cross-section. All dimensions are in mm

channels was equal to 90 mm, the inner diameter of the gas supporting tube was approximately 25 mm (Figs. 4a-c) and the height of all channels was set to 5 mm (Fig. 4d). Due to the transparency requirements of PIV measurements, all of the channels were made from a polymethylmetacrylate (PMMA) material to allow the investigated flow area to be visible. Because the melting temperature of PMMA is about 160°C, it was impossible to carry out the experiment at the high temperatures that characterize SOFC operation. The measurement process was carried out at a temperature of 293 K, and the air mixed with tracer particles was used as an experimental gas. To fulfill the dynamic similarity of flow behavior in the experimental channels, the specific flow values and corresponding Reynolds numbers were employed. According to Bedogni *et al.* (2007), the characteristic flow values of hydrogen in a circular-planar SOFC operating at 900 K are in the range of about 7.0-25.0 l/min, which after simple calculations that included the geometry of the examined

²http://www.hexis.com/index_e.htm

channels gives inlet velocities for all experimental channels in the 2.5-14.0 m/s range. The density and dynamic viscosity of hydrogen at 900 K are equal to $\rho = 0.027 \text{ kg/m}^3$ and $\eta = 18.78 \cdot 10^{-6} \text{ kg/(m s)}$, respectively (Xue *et al.*, 2005). These values result in a kinematic viscosity of $\nu = 6.90 \cdot 10^{-4} \text{ m}^2/\text{s}$. Finally, the Reynolds numbers calculated from Eq. (3.1) fall in the range from 29 to 125. Given the assigned values, the air mixture inlet flow rate to the experimental channels was set in the range of 0.1-3.0 l/min

$$\text{Re} = \frac{V d_H}{\nu} \quad (3.1)$$

The density and dynamic viscosity of air in 293 K are $\rho = 1.20 \text{ kg/m}^3$ and $\eta = 18.10 \cdot 10^{-6} \text{ kg/(m s)}$ (Wiśniewski and Wiśniewski, 2000). The calculated kinematic viscosity was equal to $\nu = 1.50 \cdot 10^{-5} \text{ m}^2/\text{s}$, resulting in the velocities of 0.0075-0.60 m/s. Thus the Reynolds numbers used during the measurements were in the range from 4 to 252, which agrees with the results calculated for hydrogen. The exact values of the investigated Reynolds numbers are presented in Table 1.

Table 1. Specific velocities and Reynolds numbers for the experimental gas in the channels inlet

Flow [l/min]	Channel 1		Channel 2		Channel 3	
	Inlet velocity [m/s]	Re	Inlet velocity [m/s]	Re	Inlet velocity [m/s]	Re
0.1	0.0075	4	0.0080	3	0.020	8
0.5	0.030	16	0.045	19	0.11	46
1.0	0.055	29	0.11	46	0.20	84
1.5	0.090	47	0.14	58	0.30	126
2.0	0.12	63	0.18	75	0.40	168
2.5	0.16	84	0.22	91	0.45	189
3.0	0.18	95	0.45	187	0.60	252

In the experiment, the air was supplied to the experimental channels from their bottom part and radially transported out (Fig. 5).

3.2. Experimental setup

The experimental setup is presented in Fig. 6. During the measurement process each channel was put separately into the experimental chamber, with the gas mixture supplied from the bottom. The light emitted by the Nd:Yag

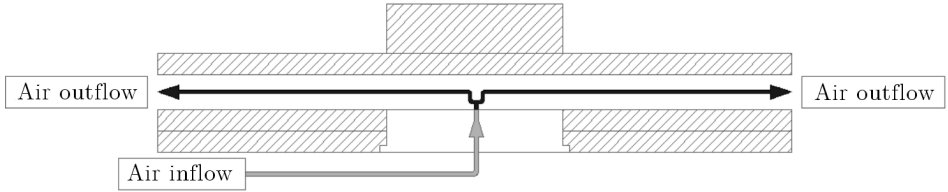


Fig. 5. Cross-section of air flow distribution in the experimental channels

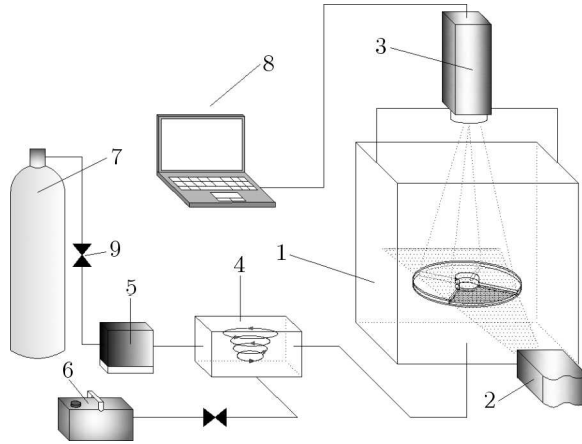


Fig. 6. 1 – Measurement chamber, 2 – Laser head, 3 – CCD camera, 4 – Mixing chamber, 5 – Mass flow controller, 6 – Smoke generator, 7 – Air container, 8 – Data acquisition system

laser illuminated the chamber through the first of the two glass windows, while the CCD camera positioned perpendicularly to the light sheet recorded the image through the second window. The remaining chamber walls were closed and painted black to avoid any undesirable laser light reflections. The air was delivered to the system from the bottle under a pressure of about 0.15 MPa and was mixed with the tracer particles in the mixing chamber. The tracer particles were generated in the smoke generator, the flow rate of air was controlled by the mass flow controller, and the particles for PIV were supplied to the channels through the controlling valve.

4. Results

During the measurement process, each channel was put into the chamber separately and the PIV measurements were carried out for all of the flow rates presented in Table 1. All of the statistical calculations were performed using

DAVIS 7.2 software. As the flow structure was assumed to be symmetrical, the PIV calculations were made only for the test sections presented in Figs. 10a-c for channels 1-3, respectively. For each flow rate, a set of 30 images was recorded. For the calculation process, the images were divided into 15 pairs of double-frame images (Fig. 7). The velocity field was calculated for each pair separately and the resulting fields averaged and the final mean velocity field distribution in the examined test section obtained. The cross-correlation function was applied for the velocity calculations and the size of the interrogation windows during iterations was set to 32×32^3 pixels.

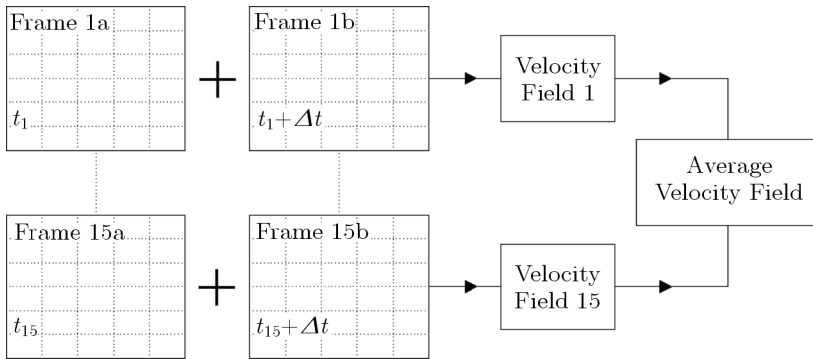


Fig. 7. Schematic representation of the PIV velocity field calculation process for the set of double frame images

4.1. Section 1

The first channel represents the simplest examined geometry, with four walls mounted radially and perpendicularly to each other (Fig. 4a). The common flow distribution in this section is presented in Fig. 8. The widening of the side walls caused the air velocity to decrease considerably. Moreover, the visualized flow is characterized by large velocity gradients in the inlet part of the channel. In order to carry out a more detailed flow structure analysis, the test section was divided into three parts, where the cross-section velocity field profiles were calculated. These cross-sections are marked in Fig. 10 and are described by planes P_1 - P_3 , where $P_n = l/l_0$ and l_0 represents the distance from the entrance to the channel and l its total axis length. The scale for each section is in a range from 0-1 and is characterized by the x/d ratio that represents a fractional position along each plane (Fig. 10d).

³The size of interrogation windows was determined based on error analysis presented in sec. 4.4.

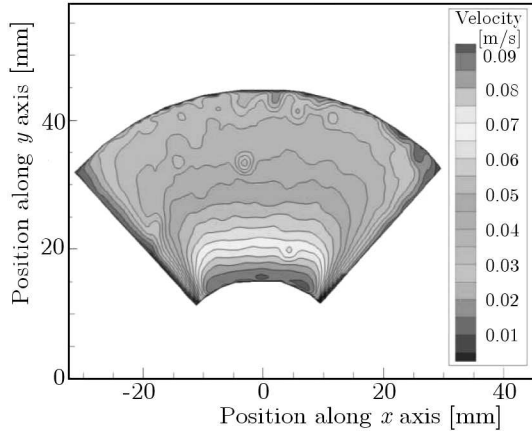


Fig. 8. Example of 2D velocity field distribution in channel 1 for the flow rate = 1.51/min

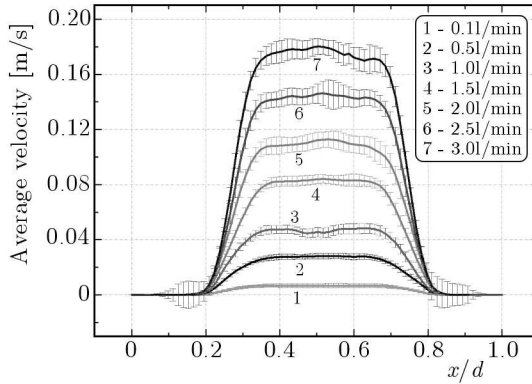


Fig. 9. Velocity field distribution at the plane P_1

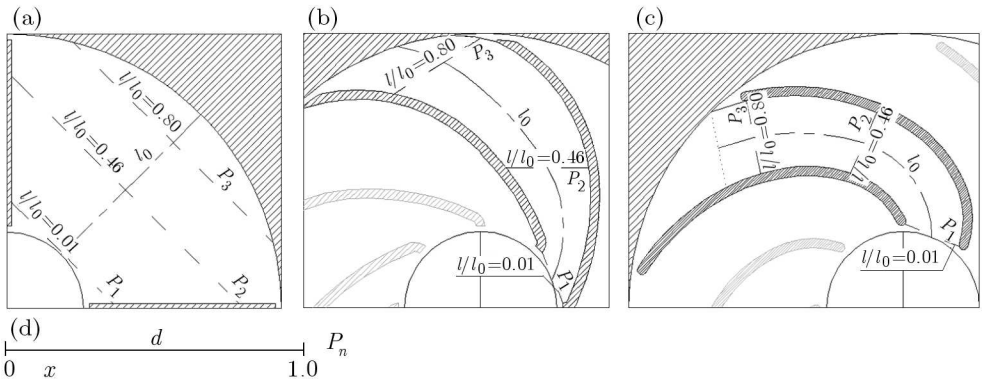


Fig. 10. Representation of the cross-section planes P_1 , P_2 and P_3 for (a) channel 1, (b) channel 2, (c) channel 3, (d) scale for each P_n plane

The velocity field distribution calculated at P_1 - P_3 planes for increasing values of the flow rate are presented in Figs. 9, 11 and 12. The figures show that the average velocity in all planes increased along with the flow rate. While the initial flow value was 0.1 l/min, the mean velocity for flow of 3.0 l/min increased by about 18, 10 and 7 cm/s for the planes P_1 , P_2 and P_3 , respectively. Most important, however, is that whereas the mean velocity values increased, the main flow in the channel began to concentrate in its middle part, which is especially evident in Fig. 11. Moreover, for high flow rates, the velocity in the outlet of the channel started to vary considerably along its horizontal axis. Additionally, as presented in Fig. 13, the mean velocities decreased substantially along the length of the channel; this is especially visible between the P_1 and P_2 planes. Table 2 presents the velocity values measured in the middle of the channel ($x/d = 0.5$) for all examined flow rates. The velocity difference between the inlet and the outlet of the channel, given by the equation $\Delta V = V_{P1} - V_{P3}$, varies from 0.37 to 10.3 cm/s and it clearly grows for higher flow rates. It may be concluded, using the results for section 1, that the flow distribution over channel 1 is highly non-uniform. The most considerable loss in velocity is particularly visible between the first P_1 and the second P_2 plane. As the aim of the paper is to find the channel geometry that provides velocity distribution that is as uniform as possible, different geometries had to be taken into consideration.

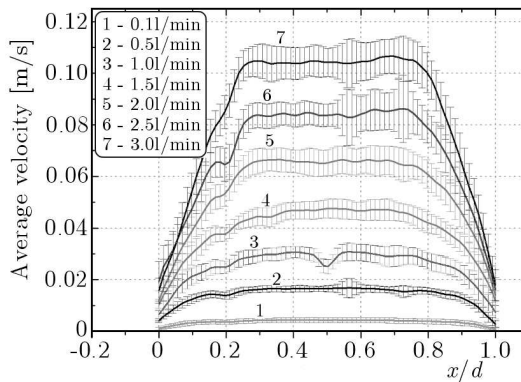


Fig. 11. Velocity field distribution at the plane P_2

4.2. Section 2

The geometry of the second analyzed channel is characterized by slight curving of its walls. We believed that this small change in the shape of each

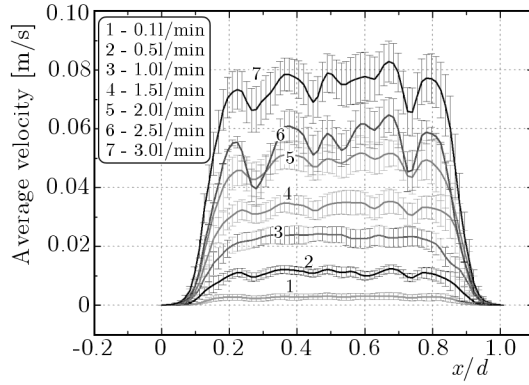
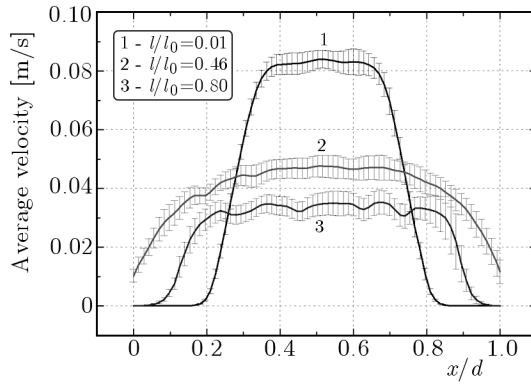
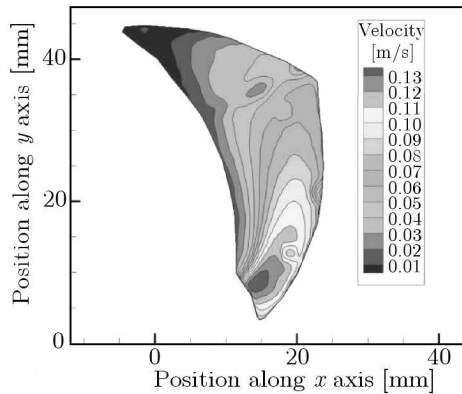
Fig. 12. Velocity field distribution at the plane P_3 Fig. 13. Example of velocity field distribution at the planes P_1 , P_2 and P_3 for the flow rate = 1.5l/min

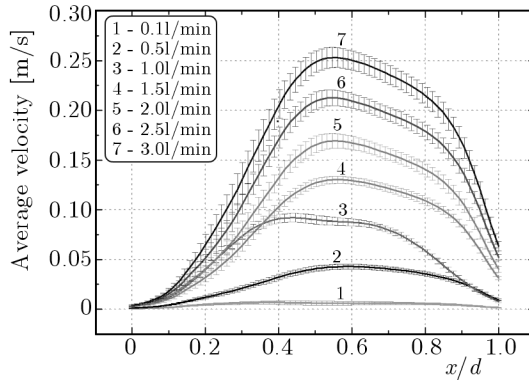
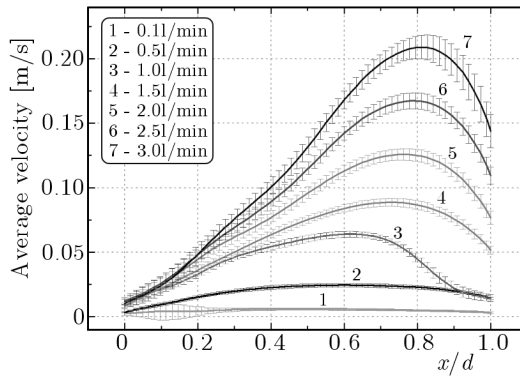
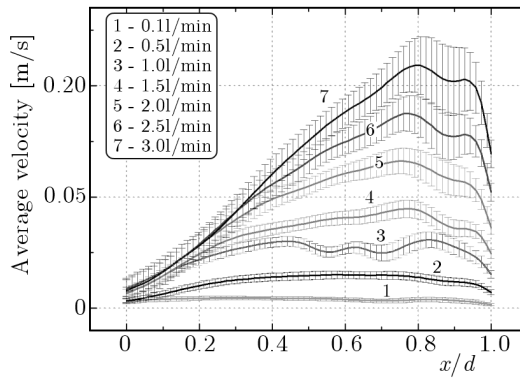
Fig. 14. Example of 2D velocity field distribution in channel 2 for the flow rate = 1.5l/min

Table 2. Velocity values in the middle of channel 1 for all P_1 - P_3 planes and flow rates

Velocity value along curve l_0							
Flow [l/min]	0.1	0.5	1.0	1.5	2.0	2.5	3.0
P_1	0.66	2.8	4.5	8.4	11.0	15.0	18.0
P_2	0.43	1.6	2.6	4.8	6.6	8.3	10.0
P_3	0.29	1.2	2.4	3.5	4.9	5.6	7.7
ΔV	0.37	1.6	2.1	4.9	6.1	9.4	10.3

channel would positively influence the velocity field distribution over the examined section. Moreover, to suppress the significant decrease in gas velocity along the channel length, the number of mounted separating walls was increased to eight, which resulted in a significant reduction of its width. The PIV measurements carried out for section 2 resulted in an exemplary velocity field distribution presented in Fig. 14. The flow in channel 2 concentrates mostly in the right part of the channel where the velocities were in the range of 8-13 cm/s.

In an effort to gain more detailed results, channel 2, like channel 1, was divided transversally by three planes; the resulting transversal velocity distribution in each plane is presented in Figs. 15-17. As in the previous case, the air velocity in channel 2 increased as the flow rate grew from 0.1 up to 3.0 l/min. The average increase in velocity was approximately 15.0, 12.0, and 6.3 cm/s for the P_1 - P_3 planes, respectively. However, as the graphs indicate, the maximum of the gas velocity has now moved to the right side of the channel. This phenomenon can be attributed to the centrifugal force strongly accelerating the gas particles and pushing them towards the outer part of the channel. Also, due to the narrowing as a result of the previous geometry, the maximum reached velocities in channel 2 are higher than those in channel 1. The average velocity decrease for the specific flow rate in channel 2 was also measured, and the obtained results of ΔV are presented in the last row of Table 3. Here it should once more be pointed out that the decrease in velocity is higher for higher flow rates and varies from 0.16 to 18.5 cm/s. While the velocity drop is higher for several flow rates than in channel 1, it is mostly caused by the significant loss in velocity at the end of the tested section. The same can also be seen in Fig. 18, where the velocity in the plane P_3 ($l/l_0 = 0.80$) is considerably lower than in the other two. Such a decrease can be largely ascribed to the proposed geometry. In the predominating part of the channel the flow is controlled by the walls, though at its end the outer wall is a little bit shorter

Fig. 15. Velocity field distribution at the plane P_1 Fig. 16. Velocity field distribution at the plane P_2 Fig. 17. Velocity field distribution at the plane P_3

than the inner one, which causes the free outflow of the air and results in a rapid decrease in velocity. On the other hand, inside the channel, mostly along its right wall, the flow is better controlled and is more homogenous than in the first geometry. This observation led to the construction of a third channel, which shall be investigated in the following Section.

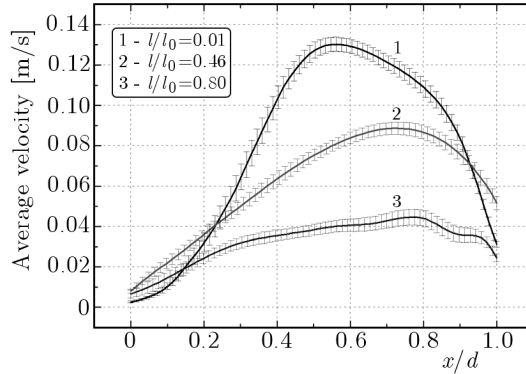


Fig. 18. Example of velocity field distribution at the planes P_1 , P_2 and P_3 for the flow rate = 1.5 l/min

Table 3. Velocity values in the middle of channel 2 ($x/d = 0.5$) for all P_1 - P_3 planes and flow rates

Flow [l/min]	Velocity value along curve l_0						
	0.1	0.5	1.0	1.5	2.0	2.5	3.0
P_1	0.59	4.3	8.9	13.0	17	21	25
P_2	0.59	2.4	6.1	7.6	9.8	12	13
P_3	0.43	1.4	3.0	3.6	5.0	5.9	6.5
ΔV	0.16	2.9	5.9	9.4	12	15	18.5

4.3. Section 3

In the preceding Section it was shown how in the last geometry the walls were strongly curved and the received channel had an almost constant width along its entire length. The number of separating walls – 8 – has not changed. Figure 19 presents an example of the obtained velocity field in the last geometry. It is immediately evident that the flow field is characterized by much higher uniformity than for the previous geometries. The regions with much lower velocities occur only in the boundary layers. Moreover, the velocities

reached in the attendant geometry are about twice higher than in the previous ones. A similar measurement process was again applied and transversal velocity characteristics were determined for each of the three illustrated planes (Fig. 10c). According to presented plots (Figs. 20-22), the average velocity difference between the lowest and highest flow rate is approximately 22, 43, 35 cm/s. What mainly matters here and is confirmed by the presented plots is the fact that in almost the entire area of the channel the velocities of the flowing gas do not decrease rapidly to very small values, as they did in the previous geometries. Thus the fuel utilization should not vary considerably in all parts of the channel. The measured average velocity decrease along the length of channel 3 is presented in Table 4 and Fig. 23. The velocity in the last geometry decreases from about 0.5 to 13.2 cm/s. However, the velocity values at $x/d = 0.5$ for the P_1 and P_2 planes are close to each other in the large part of the channels and the large drop in velocity is again caused mostly by the velocity profile in the last section. This is also observed in Fig. 23 where the transversal velocities in the planes P_1 and P_2 are close to each other in the large part of the channel. Thus this geometry shows the most promising velocity distribution and is recommended for the future cell design.

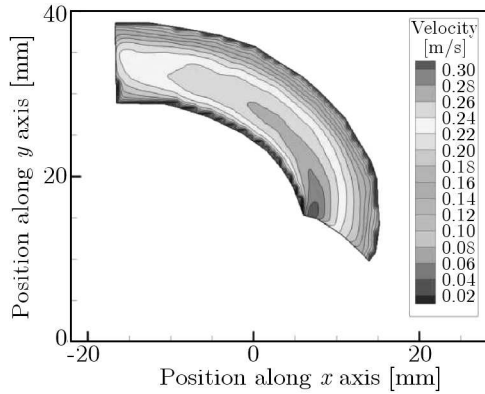
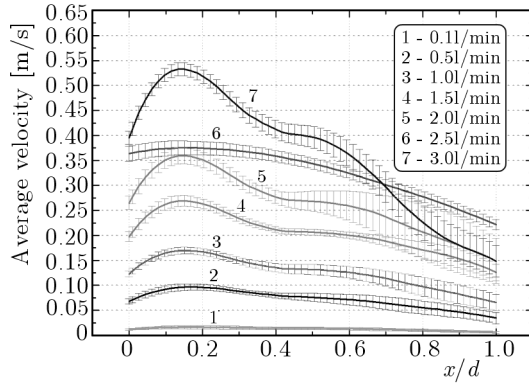
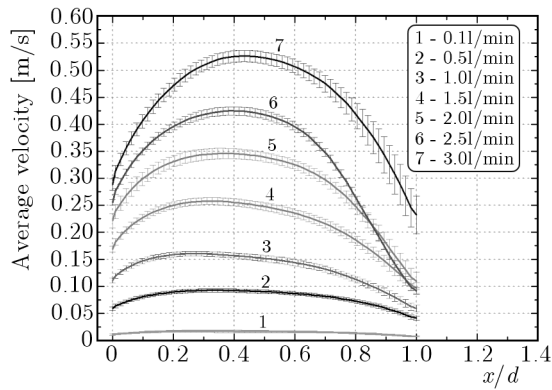
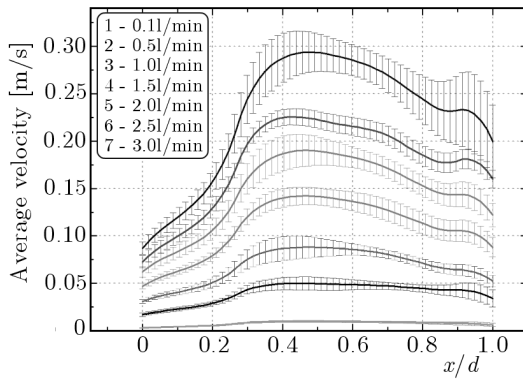


Fig. 19. Example of 2D velocity field distribution in channel 3 for the flow rate = 1.5l/min

4.4. Error analysis

According to Huang *et al.* (1997), the errors that may occur during the PIV measurements include those caused by outliers and root-mean-square errors (RMS). The outliers (spurious vectors) are velocity vectors that are easy to detect due to their corresponding velocity value which is for the most part

Fig. 20. Velocity field distribution at the plane P_1 Fig. 21. Velocity field distribution at the plane P_2 Fig. 22. Velocity field distribution at the plane P_3

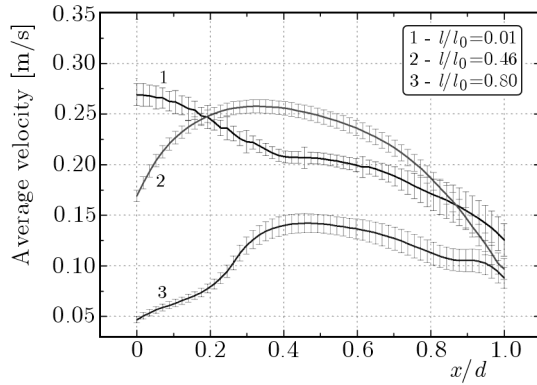


Fig. 23. Example of velocity field distribution at the planes P_1 , P_2 and P_3 for the flow rate = 1.5 l/min

Table 4. Velocity values in the middle of channel 3 $x/d = 0.5$) for all P_1 - P_3 planes and flow rates

Velocity value along curve l_0							
Flow [l/min]	0.1	0.5	1.0	1.5	2.0	2.5	3.0
P_1	1.3	7.2	13.0	21.0	27.0	33.0	36.0
P_2	1.5	8.0	13.4	21.6	28.9	33.0	44.5
P_3	0.8	4.0	6.8	11.0	14.7	17.7	22.8
ΔV	0.5	3.2	6.2	10.0	12.3	15.3	13.2

several times larger than the velocity calculated for properly distinguished particles. The main sources of these vectors are insufficient seeding density, strong particle velocity gradients along the calculation area, and strong three-dimensional flow motions as the tracer particles from the first interrogation window may move out of the laser light plane in the second window. The spurious vectors are randomly distributed and always appear in the calculation domain; practically, however, a properly prepared measurement will contain no more than 5% of these vectors (Westerweel, 1994) and they may be completely removed after the post processing stage. As the flow in the experiment was laminar with $Re \leq 252$ (see Table 1) and mostly two dimensional (as the channel length was about 6 times larger than its height), the spurious vectors had almost no influence on the calculated velocity fields. Moreover, the post-processing eliminated them in the calculation domain.

As with the PIV technique based on statistical (correlation) analysis of the recorded images, it is possible (and necessary) to calculate the RMS error of the determined velocities

$$\sigma = \sqrt{\frac{1}{n} \sum_{i=1}^n (V_i - \bar{V})^2} \quad (4.1)$$

There are several factors that influence the RMS error, including the seeding density, velocity gradients, out-of-plane particle motions, non-uniform illuminations, data acquisition noise etc. (McKenna and McGillis, 2002).

Several things have to be taken into account for the minimization of the RMS error. First of all, the proper size of the interrogation window, which will influence the number of the tracer particles that can be detected during the correlation calculations, has to be chosen. The probability of proper particle identification is higher for a large window size (assuming that the time interval between frames is properly selected) but the velocity resolution decreases with it. As the number of calculated vectors is equal to the number of interrogation windows, it is easy to predict that the resolution of the velocity field decreases 16 times as the size of the interrogation window increases from 16×16 pixels to 64×64 pixels. The effect of interrogation window size on the accuracy of calculations was studied by Hart (2000)] and Meunier and Leweke (2003). McKenna and McGillis (2002) also investigated this phenomenon and stated that the accuracy of velocities increased with an increased interrogation window size.

In the presented paper, a group of 6×6 , 12×12 , 32×32 , 64×64 and 128×128 -pixel interrogation windows in the low, medium and high flow rates have been investigated. The results of these calculations are presented in Figs. 24a-c. The interrogation window sizes that were equal to or lower than 12×12 pixels generated high statistical errors for the measured displacement of about 2.0-6.0 cm. In this regime, the calculated velocities cannot be accepted as the calculated RMS error is almost equal to or is of the same order as the measured velocity. The RMS error decreased significantly for the displacements larger than 6.0 cm but it was still much larger than the RMS error calculated for larger windows. For the interrogation window of 32×32 pixels, the RMS error decreased substantially and was in a range from 0.0-0.1 cm in the whole range of calculated displacement, which is about 5% of the measured velocity. For the large windows (64×64 , 128×128), the RMS error was even smaller but simultaneously the range of measured velocities decreased by almost twice of that for the 12×12 pixels window. It was therefore decided that the optimal size of the window for the examined system was 32×32 pixels

as it is characterized by a reasonably low RMS error and accepted range of measured velocities.

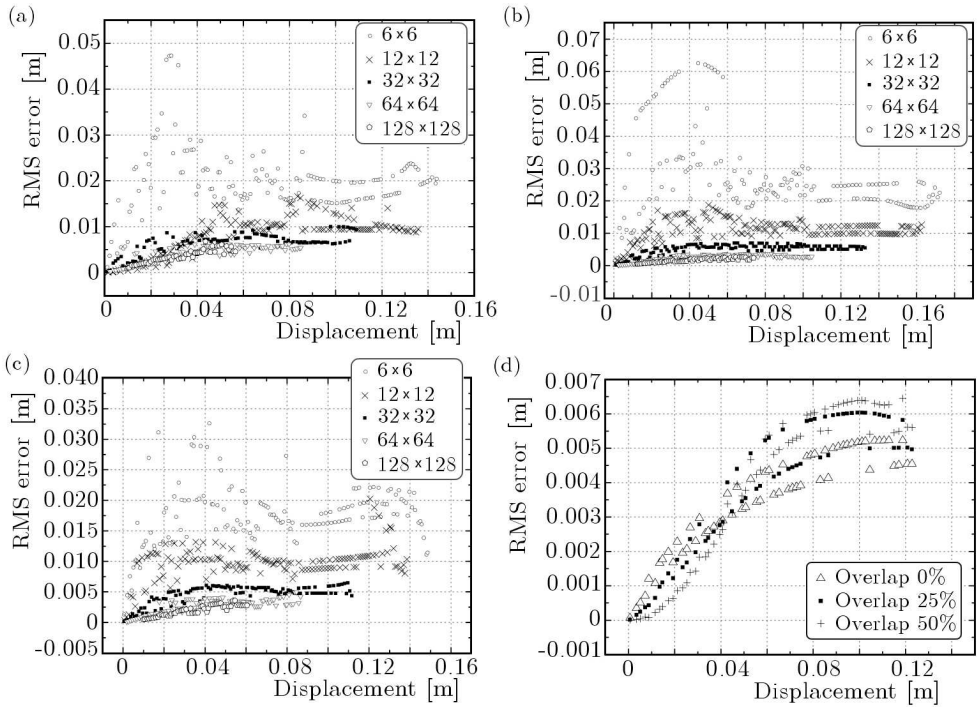


Fig. 24. (a)-(c) Influence of the interrogation window size on the accuracy of the velocity fields calculations; (a) gas flow = 0.51/min, (b) gas flow = 1.51/min, (c) gas flow = 3.01/min. (d) Various overlap factor for PIV calculation in 1.5 flow and 32×32 interrogation window size

Another important aspect in the velocity calculation is the overlap value for both interrogation windows. The overlapping technique is used to increase the velocity resolution without a change in the interrogation window size. For higher overlapping values, the resolution of measured velocities is higher but it makes the calculations less exact. Figure 24d shows that the RMS error varies with the value of the overlap factor. Moreover, the RMS error is lower for higher overlapping values if the displacement vector is less than 4-6 cm. This may be explained by the fact that for the higher overlap factor, the resultant interrogation windows are smaller, so the distance between each window is shorter and the particles moving slowly in the gas will be able to move to the second window area. Similarly, as the displacement value increases, the particles will move faster, so smaller overlap values prevent them from moving

out of the interrogation area. In Summary, choosing the proper overlap value is essential for the accuracy of PIV. The compromising value of 25% was used for the measurements in this paper to allow the accuracy and resolution of calculated velocities to be satisfied.

As Huang *et al.* (1997) showed, further improvement in the accuracy of the velocity calculations may be made by normalizing the cross-correlation function. Moreover, Anandarajah *et al.* (2006) observed that the normalization process also has a significant influence on the minimization of the partial image error (PIE). The PIE error comes from the partial image of the tracer particle in the edge of the interrogation window and is characterized by the skew of the correlation peak towards the lower values of displacement. During the normalization process the correlation function takes the form of Eq. (4.2). In the presented study, the normalization function was applied to the calculation for the 32×32 pixel window size and the overlap value of 25%. The results are presented in Fig. 25, which clearly shows that the normalization process increased

$$NCC = \frac{\sum_i \sum_j I_1(i, j) I_2(i - m, j - n)}{\sqrt{\sum_{i,j} I_1^2(i, j) \sum_{i,j} I_2^2(i, j)}} \quad (4.2)$$

the accuracy of the measurements without the loss in resolution of the measured velocities.

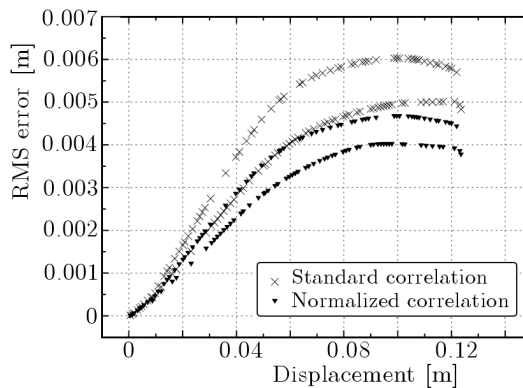


Fig. 25. The effect of correlation function normalization on the accuracy of the velocity fields calculations

It may be concluded from the above investigation that the proper choice of the correlation parameters is an important and complex problem as a wide range of parameters must be taken into account. On the other hand, the proper selection of all mentioned quantities guarantees highly accurate measurements.

5. Conclusions

Full 2D velocity field analysis of the gas flow in models of circular-planar SOFC channels has been carried out. Three different channel geometries and a wide range of flow rates, varying from 0.1 to 3.0 l/min, have been studied. For each channel, a series of plots representing the horizontal velocity distributions and examples of the 2D velocity distribution were presented. The most promising geometry for the fuel channel was represented by section 3 as the velocity field in that channel was the most uniform and had the smallest velocity gradient along its length.

As the PIV measurements represent a statistical means of calculating the velocity, the errors that appeared in the calculations were also investigated. A wide range of influencing factors including the interrogation window size, overlap value and normalization effect were tested, and the optimal values of 32×32 window size and 25% overlap with the normalization function switched on were chosen so that further calculations could be carried out.

Acknowledgements

A part of the presented work was supported by the Grant AGH No. 11.11.210.198 and by the Polish Ministry of Science under the project No. 4908/B/T02/2010/39.

References

1. ANANDARAJAH K., HARGRAVE G.K., HALLIWELL N.A., 2006, Digital image velocimetry: Partial Image Error (PIE), *Journal of Physics: Conference Series*, **45**, 174-185
2. ATKINSON A., SUN B., 2007, Residual stress and thermal cycling of planar solid oxide fuel cells, *Materials Science and Technology*, **23**, 1135-1142
3. BEDOGNI S., CAMPANARI S., IORA P., MONTELATICI L., SILVA P., 2007, Experimental analysis and modeling for a circular-planar type IT-SOFC, *Journal of Power Sources*, **171**, 617-625
4. HART D.P., 2000, PIV error correction, *Experiments in fluids*, **21**, 13-22
5. HO T.X., KOSINSKI P., HOFFMANN A.C., VIK A., 2008, Numerical study of an SOFC with direct internal reforming using charge diffusion-based model, *Proceeding of the 8th European SOFC Forum Lucerne*, 1-13
6. HUANG H., DABIRI D., GHARIB M., 1997, On errors of digital particle image velocimetry, *Meas. Sci. Technol.*, **8**, 1427-1440

7. XUE X., TANG J., SAMMES N., DU Y., 2005, Dynamic modeling of single tubular SOFC combining heat/mass transfer and electrochemical reaction effects, *Journal of Power Sources*, **142**, 11-222
8. KEANE R.D., ADRIAN R.J., 1992, Theory of cross-correlation analysis of PIV images, *Applied Scientific Research*, **49**, 191-215
9. LAURENCIN J., MOREL B., BULTEL Y., LEFEBVRE-JOUD F., 2006, Thermo-mechanical model of solid oxide fuel cell fed with methane, *Fuel Cells*, **6**, 64-70
10. LEWIS J.P., 1995, Fast template matching, *Vision Interface*, 163-165
11. MCKENNA S.P., MCGILLIS W.R., 2002, Performance of digital image velocimetry processing techniques, *Experiments in Fluids*, **32**, 106-115
12. MELLING A., 1997, Tracer particles and seeding for particle image velocimetry, *Measurement Science and Technology*, **8**, 1407-1416
13. MEUNIER P., LEWEKE T., 2003, Analysis and treatment of errors due to high velocity gradients in particle image velocimetry, *Experiments in Fluids*, **35**, 408-421
14. RAFFEL M., WILLERT C., 2007, *Particle Image Velocimetry: Practical Guide*, Springer Verlag, Berlin Heidelberg
15. SINGHAL S.C., KENDALL K., 2006, *High Temperature Solid Oxide Fuel Cells: Fundamentals, Design and Applications*, Elsevier, Amsterdam
16. WESTERWHEEL J., 1994, Efficient detection of spurious vectors in particle image velocimetry data, *Experiments in Fluids*, **16**, 236-247
17. WESTERWHEEL J., 1997, Fundamentals of digital particle image velocimetry, *Measurement Science and Technology*, **8**, 1379-1392
18. WIŚNIEWSKI S., WIŚNIEWSKI T.S., 2000, *Wymiana ciepła*, Wydawnictwo Naukowo-Techniczne, Warszawa

Analiza eksperymentalna struktury przepływu gazu w zróżnicowanych geometriach kanału paliwowego ogniwa paliwowego typu SOFC

Streszczenie

W zaprezentowanej artykule, tematem realizowanych badań jest analiza eksperymentalna struktury przepływu gazu w trzech modelach kanałów transportowych ogniwa paliwowego typu SOFC (*Solid Oxide Fuel Cell*). Celem badań było zaproponowanie geometrii kanału, która pozwoliłaby utrzymać jednorodny rozkład pola prędkości na powierzchniach elektrod w rzeczywistych warunkach pracy ogniwa. Dobrej odpowiedniej geometrii kanałów transportowych jest istotny z punktu widzenia

wydajności oraz bezpieczeństwa pracy ogniwa, ponieważ bezpośrednio wpływa na wydajność reakcji elektrochemicznych zachodzących w ogniwie oraz na rozkład temperatury w jego wnętrzu, uwarunkowany silnie egzotermicznymi reakcjami elektrodowymi oraz w przypadku wykorzystania paliwa węglowodorowego dodatkową, endotermiczną reakcją reformingu i egzotermiczną reakcją tlenku węgla z parą wodną.

Na potrzeby eksperymentu zaprojektowano oraz wykonano z pleksi trzy przykładowe geometrie kanałów przepływowych. Badania eksperymentalne przeprowadzono w temperaturze pokojowej. Gazem wykorzystanym w badaniach było powietrze. Bazując na teorii podobieństwa ustalono wartości liczby Reynoldsa na poziomie odpowiadającym wielkościom literaturowym, dzięki czemu otrzymane wyniki można traktować jako wiarygodne i oddające charakter przepływu paliwa w rzeczywistym ogniwie paliwowym. Profile prędkości wyznaczono wykorzystując bezinwazyjną metodę *Particle Image Velocimetry*. Ponadto, na podstawie analizy błędów określono zestaw parametrów obliczeniowych, dla których wyznaczone pole wektorowe charakteryzowało się największą dokładnością.

Manuscript received September 13, 2010; accepted for print December 9, 2010